ELSEVIER

Tectonophysics 333 (2001) 261–276

TECTONOPHYSICS

www.elsevier.com/locate/tecto

Three-dimensional modeling of the behavior of the oblique convergent boundary of southeast Taiwan: friction and strain partitioning

Jyr-Ching Hu[a,*], J. Angelier[b], C. Homberg[b], Jian-Cheng Lee[c], Hao-Tsu Chu[d]

[a]*The Institute for Secondary School Teachers in Taiwan, 67, Tsu-Fang Street, Feng-Yuan, Taichung, 42027, Taiwan, ROC*
[b]*Département de Géotectonique, Tectonique Quantitative, Université Pierre et Marie Curie, 4 pl. Jussieu, 75252 Paris Cedex 05, France*
[c]*Institute of Earth Sciences, Academia Sinica, P.O. Box 1-55, Nankang, Taipei, Taiwan, ROC*
[d]*Central Geological Survey, P.O. Box 968, Taipei, Taiwan, ROC*

Abstract

The Longitudinal Valley Fault (LVF) of eastern Taiwan is the plate boundary between the Philippine Sea plate and Eurasian plate. Analyses of triangulation networks showed that two distinct deformation zones coexist: thrusting prevails between the Pinanshan Conglomerate massif and the Central Range to the west, while strike-slip dominates between the Pinanshan massif and the Coastal Range to the east. Crustal deformation and displacement partitioning along this oblique convergence boundary is investigated by using a 3D distinct-element model. To constrain our models, we take into account the present-day deformation of southern LVF based on geodetic data. Particular attention is paid to the role of the major faults that play an important role in the distribution of the regional strain patterns.

The overall deformation is examined by separating the transverse and lateral components of the regional deformation. Our models predict that both the dip-slip and strike-slip increase as the friction coefficient decreases in the eastern fault between Coastal Range and Pinanshan Conglomerate massif. For the western fault between Central Range and Pinanshan Conglomerate massif, the dip-slip increases when the friction coefficient decreases. Conversely the strike-slip decreases as the friction coefficient decreases. The model that provides the best fit in the eastern fault has an effective coefficient in the range of 0.1–0.4. The friction coefficient of 0.27 predicts a strike-slip slip of 20.5 mm/yr, similar to the rate of 22 mm/yr towards N353°E calculated from geodetic data. Along the western fault, the models that provide the best fit have a friction coefficient of 0.8–1.0. These models predict the average fault-normal shortening of about 15.7 mm/yr. The displacement mentioned above is a 30% larger than that of geodetic measurements. Internal deformation by numerous minor faults inside the Pinanshan Conglomerate massif accounts for the discrepancy between the model-predicted and the observed displacement rate. Our models predict an average displacement rate of about 33 mm/yr towards N318°E for reasonable values of the coefficient of friction. These results are consistent with the displacement rate of 28 ± 8 mm/yr towards N329 ± 10°E between the Coastal Range and the Central Range based on the trilateration networks around the southern Longitudinal Valley. The friction parameters do affect the orientation and magnitude of slip along faults by a series of parametric studies. We conclude that the strain partitioning of crustal deformation of southern LVF strongly depends on the orientation of oblique convergence, the geometry of faults, and their friction coefficients. Taking into account both the simplified assumptions of the 3D numerical simulation and the uncertainties of geodetic measurements, our estimates of friction parameters along major discontinuities are only valid to first order.

Keywords: strain partitioning; Taiwan; distinct-element model

* Corresponding author. Tel.: +886-4-2522-7929, ext. 115; fax: +886-4-2520-5528.
E-mail address: jchu@ultra.isst.edu.tw (J.-C. Hu).

0040-1951/01/$ - see front matter
PII: S0040-1951(00)00278-X

1. Introduction

In a strain-partitioned system accommodating oblique convergence (transpression), the relative motion is commonly distributed along two parallel faults, a strike-slip fault and a thrust fault that, respectively, accommodate most of margin-parallel and margin-perpendicular motions (e.g. Fitch, 1972). Regions of decoupling of active transpressive faulting are often characterized by major strike-slip faults and associated compressional structures, which generally show a high angle between the principal stress direction and the major fault orientation. Analyses of stress fields (e.g. Mount and Suppe, 1987) effectively revealed the common presence of decoupling across active transpressive plate boundaries, such as the San Andreas Fault, the Great Sumatran Fault, the Alpine Fault, and the Philippine Fault. In this paper, we present 3D numeric simulations of strain partitioning, based on a case study along the active suture zone of eastern Taiwan where decoupling occurs. Partitioning in this area is caused by the oblique convergence between the Luzon island–arc system of the Philippine Sea plate and the Chinese continental margin of the Eurasian plate (Fig. 1a). Recent GPS measurements of the station velocity between the islands of the Philippine Sea plate (Lutao and Lanhsu) and the Taiwan Strait (Penghu) revealed a velocity of 8.2 cm/yr in the N309°E direction (Yu et al., 1997).

The Longitudinal Valley Fault (hereafter referred to as LVF) is the surface expression of a major shear zone striking about N20°E, dipping approximately 55° to the ESE, which can be followed along strike over a distance of about 160 km. The amount of oblique slip on the fault is larger than 20 mm/yr (Yu et al., 1990; Lee and Angelier, 1993), and has both a thrust and a left-lateral component. The deformation zone accounts for about 25–30% of the total plate convergence (Angelier et al., 2000).

Analyses of repeated trilateration data (Yu et al., 1990) revealed significantly different slip vectors along the LVF (Fig. 2a). At the northern tip, near Hualien, the LVF is a strike-slip fault with left-lateral slip of about 23 mm/yr (Yu et al., 1990). In the middle part, from Juisui to Chihshang, the LVF acts as a left-lateral reverse fault (2/3 of transverse component and 1/3 of strike-slip component) with about 21 mm/yr of oblique horizontal shortening (Lee and Angelier, 1993). In the southern part, the LVF shows a total horizontal shortening of 34 mm/yr (Yu et al., 1990). A recent study in this area (Lee et al., 1998) showed that the oblique shortening in this region is accommodated along two branches of the LVF, a reverse fault and a strike-slip one (Fig. 2b), on both sides of the Plio-Pleistocene molasse deposits (Pinanshan Conglomerate) between the Central Range and the Coastal Range.

In this paper, we aim at characterizing the active deformation field in the southern part of the LVF. We use a three-dimensional (3D) distinct-element numerical modeling approach. We restrict our study to the largest and most active discontinuities, where constraints can be clearly defined and validated with geological data. We thus combine a 3D numerical simulation with the knowledge of the deformation pattern from geodetic measurements and geological constraints, in order to check the mechanical validity of the observed distribution of deformation and to estimate the mechanical consistency of the frictional behavior.

2. Geological framework

The Longitudinal Valley separates the mountains of Central Range and the Coastal Range of Taiwan (Fig. 1b). In the Coastal Range, principally composed of Miocene calc-alkaine volcanic formations of the northern Luzon arc overlain by Plio-Pleistocene flysch-type deposits, numerous west-vergent thrusts trend NNE–SSW. The heavily sheared Lichi Mélange crops out on the eastern bank of the Pinantachi River whereas the Pinanshan Conglomerate is exposed to the west (Fig. 1b). The pre-Neogene metamorphic rocks of the Central Range crop out west of the LVF, with low grade Paleogene slates and quartz–feldspars metasandstones underlain by the Pre-Tertiary high grade Tananao complex composed of marbles, greenschists, quartz–mica schists, and granitoid rocks. The metamorphic foliation strikes NNE–SSW and dips moderately to the west in the study area.

The Pinanshan Conglomerate (Fig. 1b) is composed of coarse fluvial sediments (Page and Suppe, 1981) that accumulated at the foot of the Central Range. The material derived from the metamorphic units of the

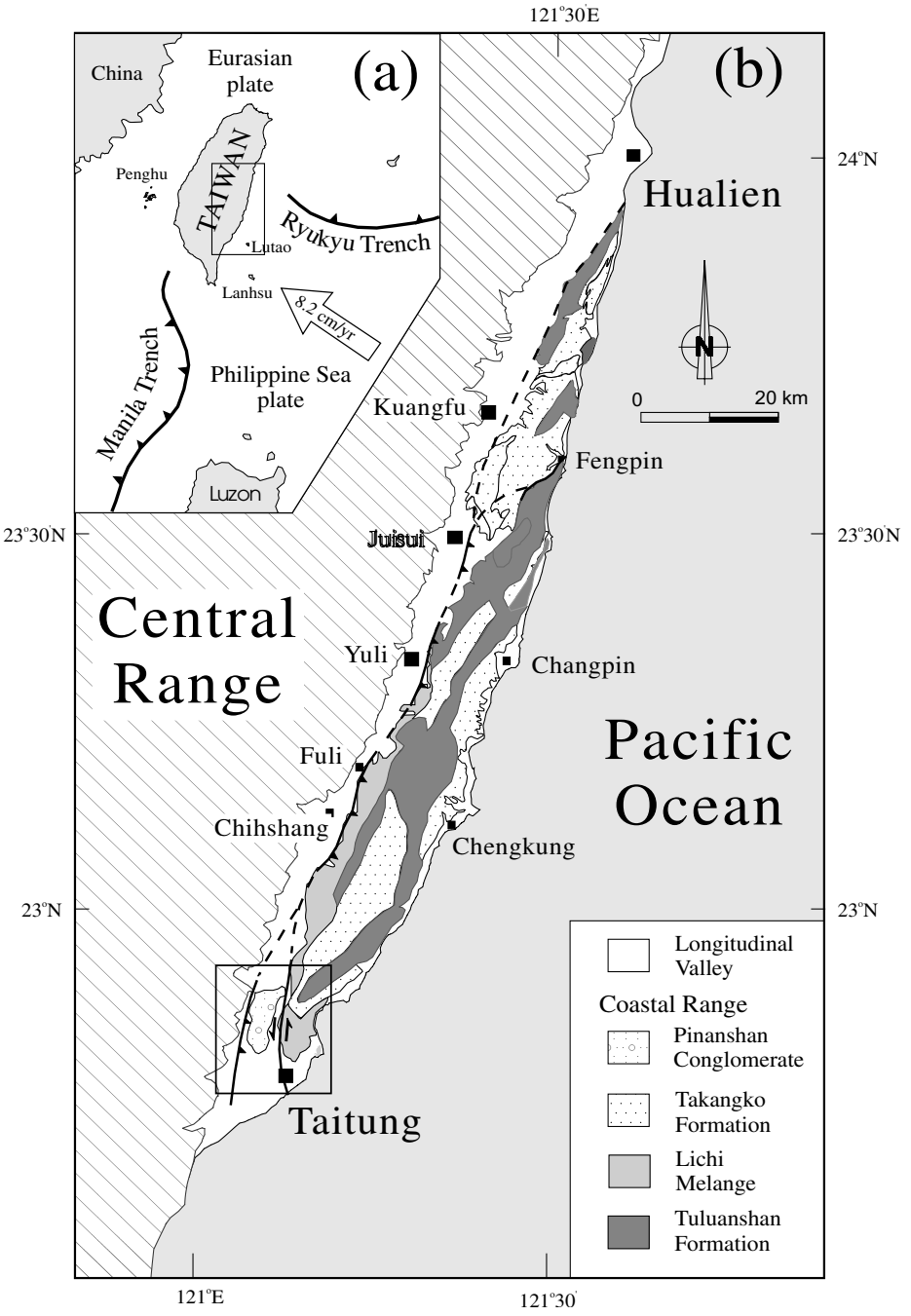

Fig. 1. (a) Convergence between the Philippine Sea plate and the Eurasian plate in the Taiwan area. Open arrow indicates the relative vector across Taiwan island with 8.2 cm/yr towards N309°E (Yu et al., 1997). (b) General geological map of the Coastal Range in eastern Taiwan. Thick solid and dashed lines represent the traces of the LVF.

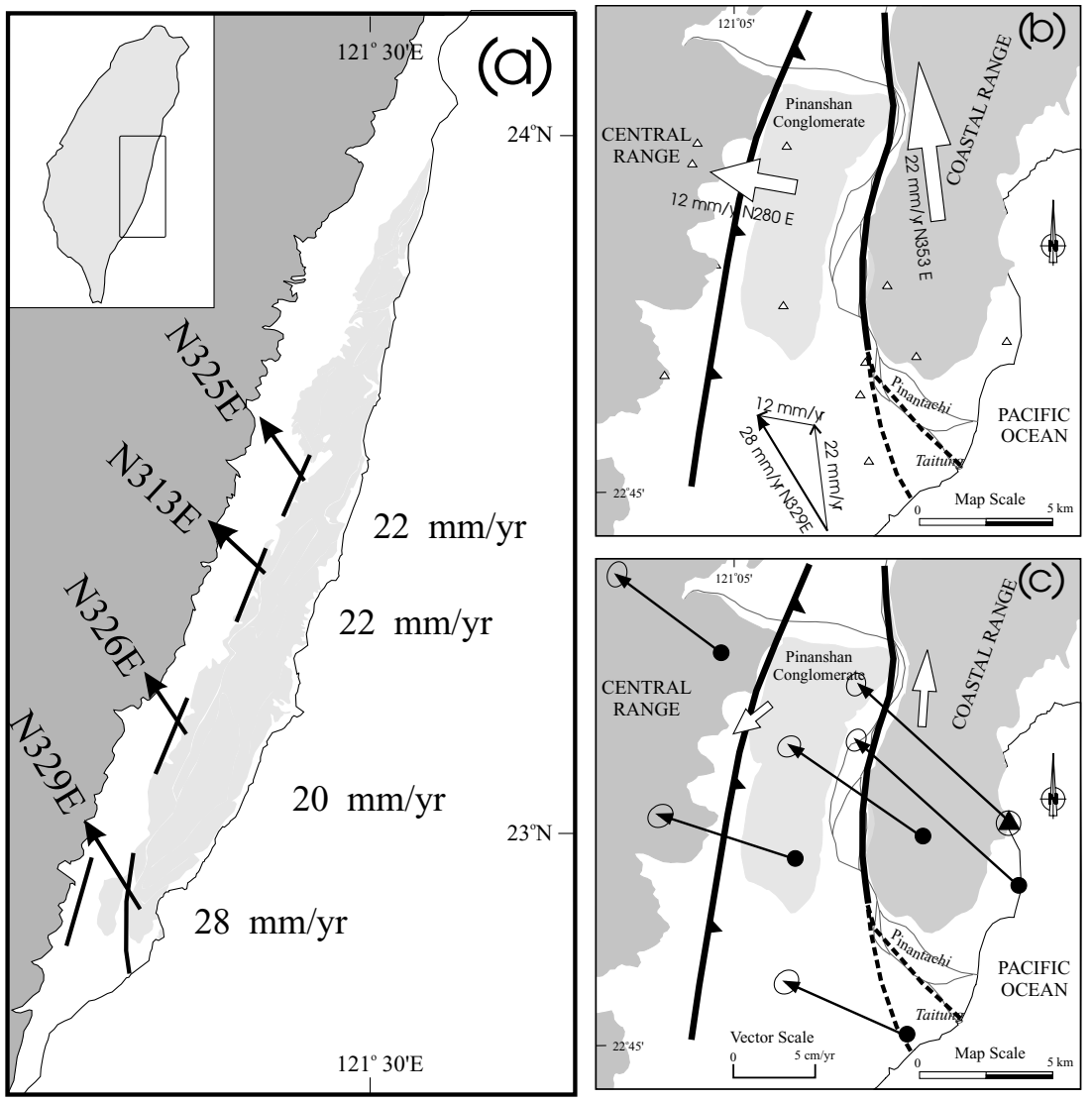

Fig. 2. Simplified geological of the Pinanshan area and main results from trilateration network analyses and GPS data. (a) Application of model of discontinuous deformation along the LVF (Lee and Angelier, 1993). Arrows indicate displacements of the upthrust, eastern block of the LVF relative to the Central Range. (b) Crustal deformation involves two major faults on both sides of the Pinanshan Conglomerate massif. Open triangles indicate the stations of trilateration. Large open arrows indicate the motion of each block relative to the block adjacent to the west. Thin arrows show the velocity triangle giving the motion of the eastern block relative to the western one. (c) GPS station velocities in southern Longitudinal Valley relative to Paisha, Penghu after Yu et al. (1997). The 95% confidence ellipse is shown at the tip of each velocity vector. Solid triangle inside circle indicates permanent stations; solid circles indicate temporary stations. Thick lines show major faults zones.

Central Range, but some pebbles from the Coastal Range are present, indicating that deposition between these two ranges. The age of the formation is Quaternary, but in more detail remains uncertain. The Pinanshan Conglomerate constitutes an asymmetrical syncline with a steep, nearly vertical, eastern limb, in fault contact with the metamorphic rocks of the Central Range to the west and the Lichi Mélange of the Coastal Range to the east.

Barrier et al. (1982) first identified pre- and

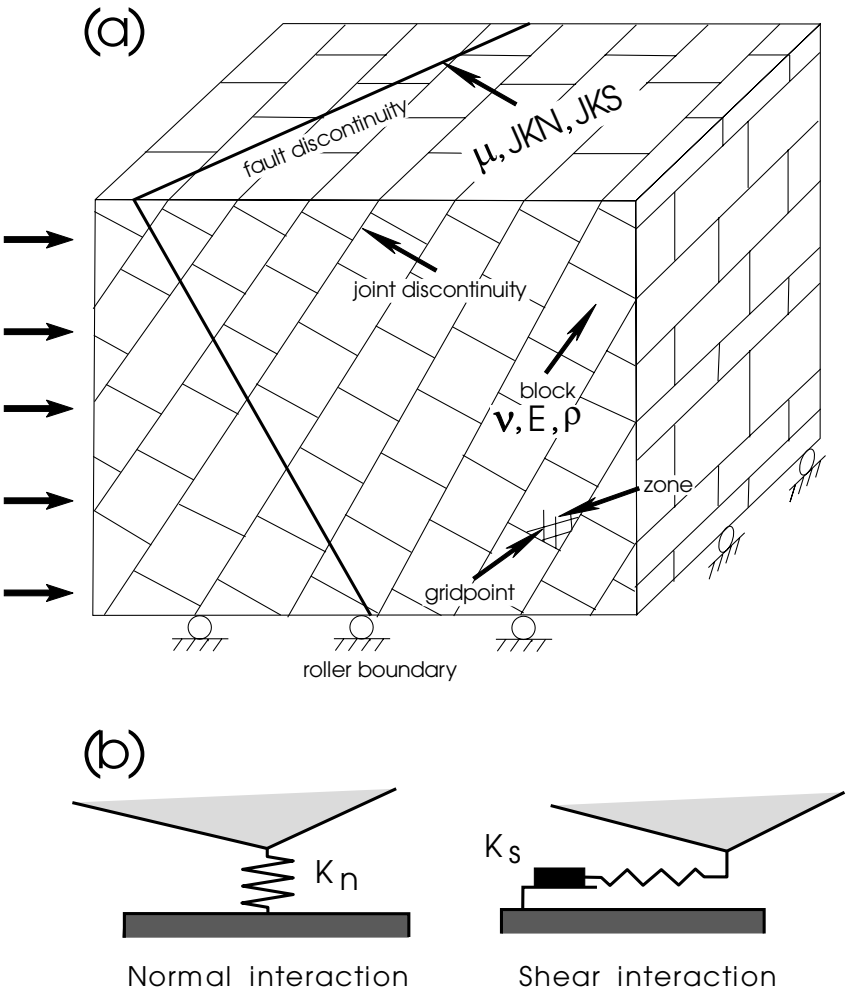

Fig. 3. Basic scheme of the 3D distinct-element method. (a) Schematic diagram of a distinct-element model. Mechanical properties of block medium: ρ (density), E (Young's modulus) and ν (Poisson's ratio). Mechanical properties of the discontinuity: μ friction coefficient), JKN and JKS (normal and shear stiffnesses). (b) Mechanical representation of interface behavior in the distinct-element method.

post-folding strike-slip faulting of the Pinanshan Conglomerate, indicating N100–105°E compression nearly perpendicular to the N–S to NNE–SSW fold axis. In aerial photographs, two dense sets of fractures, trending N140°E and N70°E, are consistent with the trends of conjugate strike-slip faults. This density of strike-slip faults is not surprising in light of the geodetic results suggesting present-day deformation within the conglomerate. South of the Pinanshan Conglomerate, its boundary faults disappear beneath the Taitung plain and offshore. To the north of the Pinanshan Conglomerate, the two faults merge into a single major fault, the LVF, where shear deformation concentrates in a very narrow zone (Angelier et al., 1997).

3. Geodetic data and active deformation

The active deformation of the area is accurately known from geodetic studies (Fig. 2). A trilateration network covering the southernmost portions of the LVF and Coastal Range in the Taitung area was surveyed nine times from 1983 to 1990 (Yu et al.,

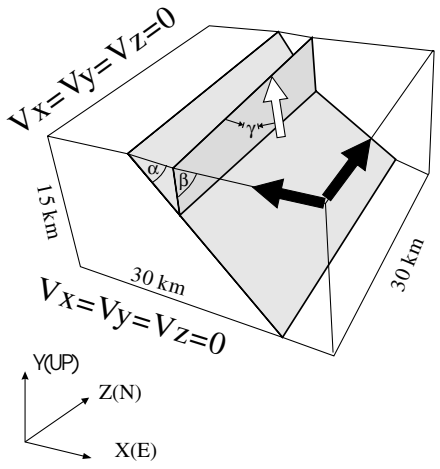

Fig. 4. 3D block diagram showing the geometry and discretization of the model. The width (z), length (x) and depth (y) of the model are 30, 30, and 15 km, respectively. Shaded surfaces define two zones of weakness (faults) having properties of mechanical discontinuity as defined in Fig. 3 and Table 1. Young's Modulus is 60 GPa for all subdomains. Poisson's ratio is uniform, 0.25. Solid arrows indicate displacement defined as boundary conditions (based on GPS, see Fig. 2c). Open arrow in the horizontal plane indicates the obliquity of block convergence (at an angle γ relative to fault trend). The dip angles of the western thrust fault and the eastern strike-slip fault are α and β, respectively. Reference frame X, Y and Z are shown.

1992). Lee et al. (1998) illustrated the characteristics of deformation along highly localized active fault zones. As a good approximation of the deformation, one can consider the relative movement of rigid blocks separated by rectilinear faults (Lee and Angelier, 1993). In the area studied, two major active faults divide the area into three blocks: the Central Range, the Pinanshan Conglomerate massif, and the Coastal Range (Fig. 2). The geodetic data indicate that the Pinanshan Conglomerate massif moves westward toward the Central Range at a rate of 12 ± 3 mm/yr towards N280 $\pm$ 20°E, and that the Coastal Range moves northward relative to the Pinanshan Conglomerate massif at a rate of 22 ± 5 mm/yr towards N353 $\pm$ 7°E (Fig. 2b). Accordingly, the total displacement between the Central Range and the Coastal Range is 28 ± 8 mm/yr towards N329 $\pm$ 10°E (Fig. 2b).

Based on strain tensor analysis, Lee et al. (1998) showed that the crustal deformation in the area of the Taitung trilateration network illustrates two different styles east and west of the Pinanshan massif. On the western side, E–W to ESE–WNW horizontal shortening occurs between the stations in the Pinanshan Conglomerate and the Central Range, consistent with thrusting across the N–S-trending boundary fault (Fig. 2b). The eastern part of the network showed a variety of strain tensors, with NW–SE shortening and NE–SW elongation, consistent with transpression and left-lateral slip along the N–S fault line between the Coastal Range and the Pinanshan Conglomerate. The strain tensors in the southern Longitudinal Valley are thus consistent with the hypothesis of partitioning.

We also considered the results of recent GPS determinations (Yu et al., 1997) around the Pinanshan area (Fig. 2c) to constrain our model in terms of displacement vectors. Note that these displacements are given relative to the Taiwan Strait, whereas the earlier conventional data used a local frame. The results, however, are generally similar.

4. Numerical modeling method

The distinct-element method is a numerical method in geomechanics and pre-fractured geological domains that enable one to simulate the mechanical response of systems composed of discrete blocks. This method falls within the general classification of discontinuum analysis techniques. A discontinuous medium is distinguished from a continuous medium by the existence of interfaces or contacts between the discrete elements that constitute the system. Many authors (e.g. Hart et al., 1988; Harper and Last, 1990) have published detailed descriptions of the numerical schemes. The detailed description of the 3DEC computer code is beyond the scope of this paper. Several modeling experiments have documented the ability of this method to solve geological problems involving fault behavior (Dupin et al., 1993; Hu et al., 1997, 2001).

The distinct-element method is based on a time marching integration scheme using central finite difference. It is an explicit method in which the equations of dynamics (e.g. Newton's second law for rigid body) are integrated over time. Within the distinct-element method, a rock mass consists of a system of discrete blocks with mechanical interaction at their boundaries (Fig. 3). Block interactions are

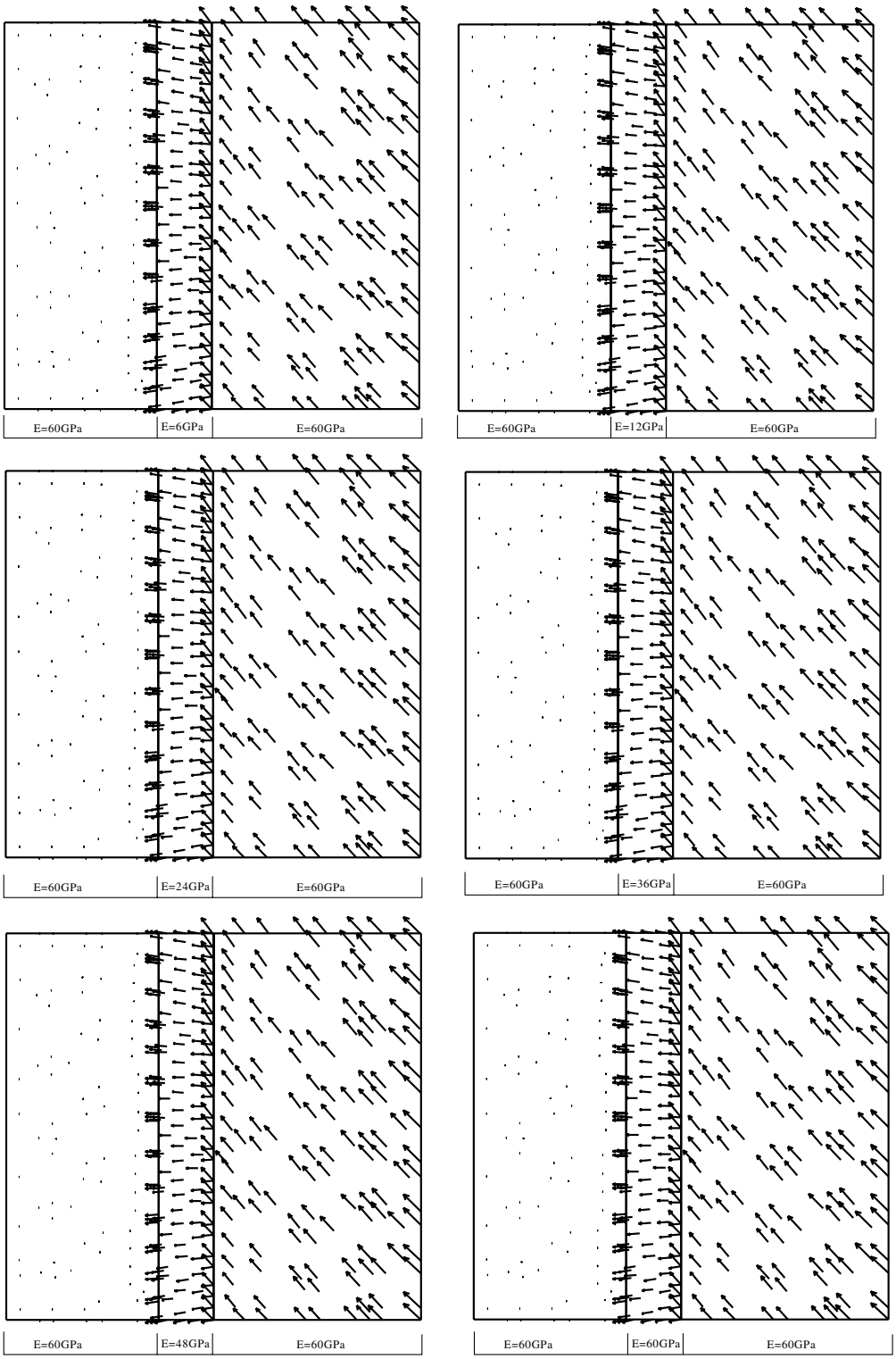

Fig. 5. Computed velocity field with a variety of Young's moduli to explore the sensitivity of in mechanical parameters. Poisson's ratio is 0.25 for all subdomains. Boundary condition is the same as Fig. 4.

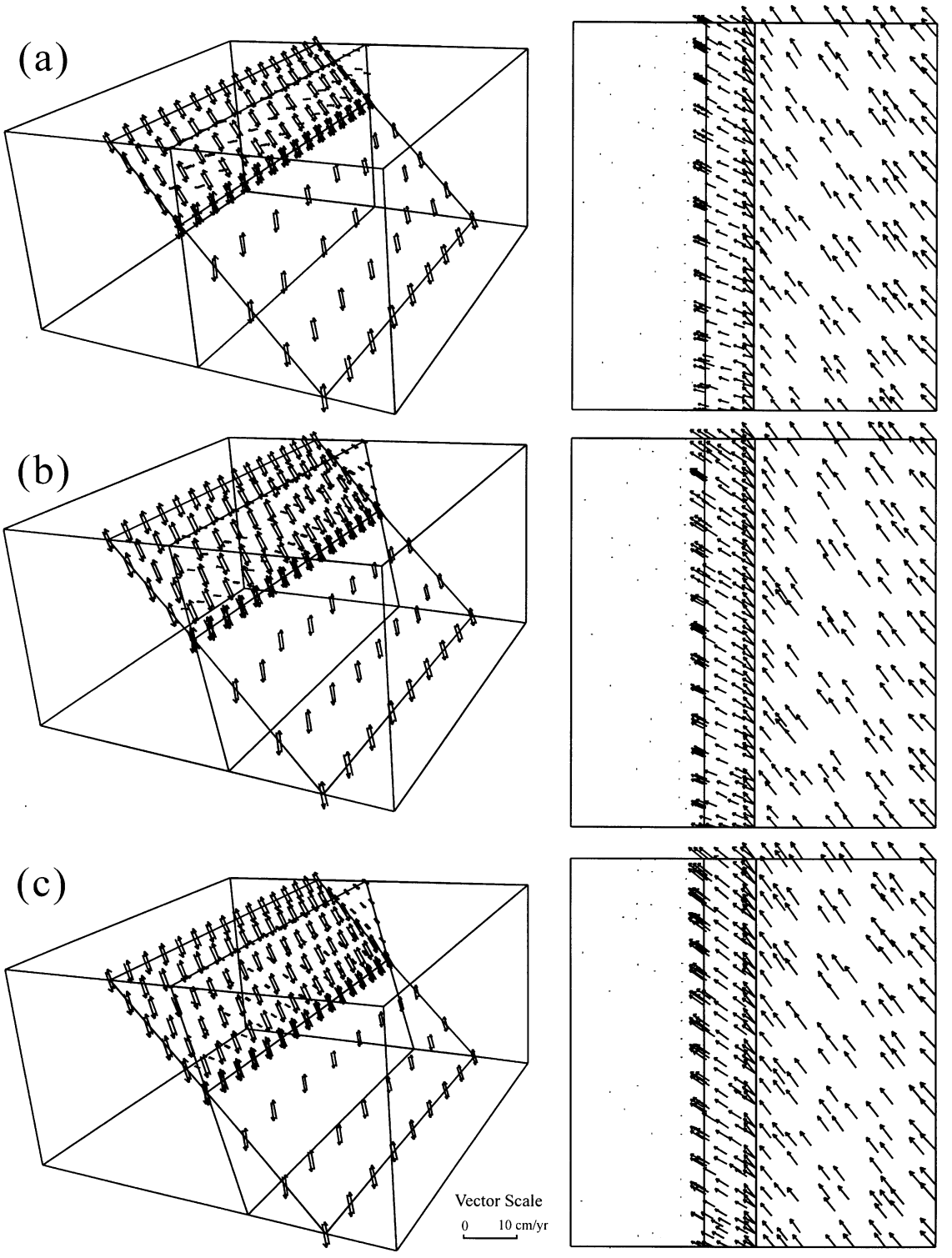
(a)
(b)
(c)
Vector Scale
0 10 cm/yr

computed assuming finite stiffness at contact points along the interface between blocks. The vertices of the finite tetrahedra zones located along the discontinuities are the contact points between blocks. The contact forces applied to rigid blocks or discrete particles are given by the elastic response at contact points that are evaluated after each integration cycle over the time step. Opening or shear displacement along block interfaces occurs when the normal and the shear forces meet conditions for tensile or shear failure, respectively. The shear strength is defined by a Mohr–Coulomb failure criterion.

5. The 3D model of convergent boundary

As major targets, we considered the major shear zones of the southern LVF (Figs. 1 and 2). Numerous models were calculated, with different fault dips and friction values. Our basic model (Fig. 4) included three subdomains with the same block material properties. Models with different block properties were used for comparison purposes. We considered the two major faults presented before (Figs. 1 and 2), and we neglected the minor faulting and the folding within the Pinanshan Conglomerate. The kinematic boundary conditions were based on the geodetic information summarized in Fig. 2. It should be noted that the uncertainties on vertical velocities are at least three times larger than those on horizontal velocities (e.g. Hofmann-Wellenhof et al., 1997). For this reason, we only used the horizontal components to constrain our models.

In our modeling, the motion of the medium is controlled by Newton's second law. Deformation is continuous and linear elastic in the blocks. The blocks shown in Fig. 4 are considered homogeneous and isotropic, and their mechanical properties are listed in Table 1. Sliding along discontinuities is allowed and controlled by a linear force–displacement law and shear stresses along the discontinuities obey the Mohr–Coulomb failure criterion. As a result, the required parameters to solve the calculation are the coefficient of friction, the cohesion the normal and shear stiffnesses of the discontinuities and the density and elastic constants of the blocks (Table 1).

Because the elastic parameter of the blocks is not well constrained, we calculated models with a variety of Young's moduli and Poisson's ratios, in order to explore the sensitivity of our results to changes in these parameters. Although the elastic parameters finally retained should be regarded somewhat arbitrary, we found that within acceptable ranges elastic parameters for deformable blocks (Turcotte and Schubert, 1982), the patterns of velocity fields had very little sensitivity to the absolute elastic values and were moderately influenced by the ratios of these parameters. To illustrate this aspect, we present the results of few experiments carried out with the same boundary conditions and contrasting ratios between Young's moduli of the blocks (Fig. 5). Concerning other technical aspects, experiments with different time-steps and deformation velocities showed that such parameters did not influence our results significantly. These preliminary experiments allowed us to subsequently concentrate on the behavior of the discontinuities that we were principally interested in.

We explored the effect of friction on faults by running a series of models with single fault geometry and coefficients of friction of 1.0, 0.8, 0.6, 0.4, 0.27, 0.1 and 0.01. Young's modulus is uniform in all models (60 GPa). A uniform Poisson's ratio (0.25) was adopted. The actual fault dip is uncertain and may deviate from the vertical surface by about 10–20°. Consequently, we used models with a variety of dip angles (90°, 80°E and 70°E). For dip angle of 90°, the strike-slip is about 21 mm/yr; when the dip is 70°E, the strike-slip decreases to 11 mm/yr. Not surprisingly, the displacement partitioning with the vertical fault is more prominent than for 80°E and 70°E dip angles (Fig. 6).

The present-day overall deformation around the LVF can be examined by distinguishing the transverse and lateral components of the regional deformation. We made a variety of models in order to check the influence of the uncertainties in the GPS/trilateration

Fig. 6. 3D Perspective view (on left) of shear displacements and plane view of surface deformation (on right) obtained with a variety of dip angles for the eastern fault (β): (a) 90°; (b) 80°; and (c) 70°. Dip angle in western fault (α) is 45°. Computed velocity vectors as thin arrows. Shear displacement vectors as pairs of thin arrows (on left). Velocity vectors shown for both sides of each discontinuity (on right).

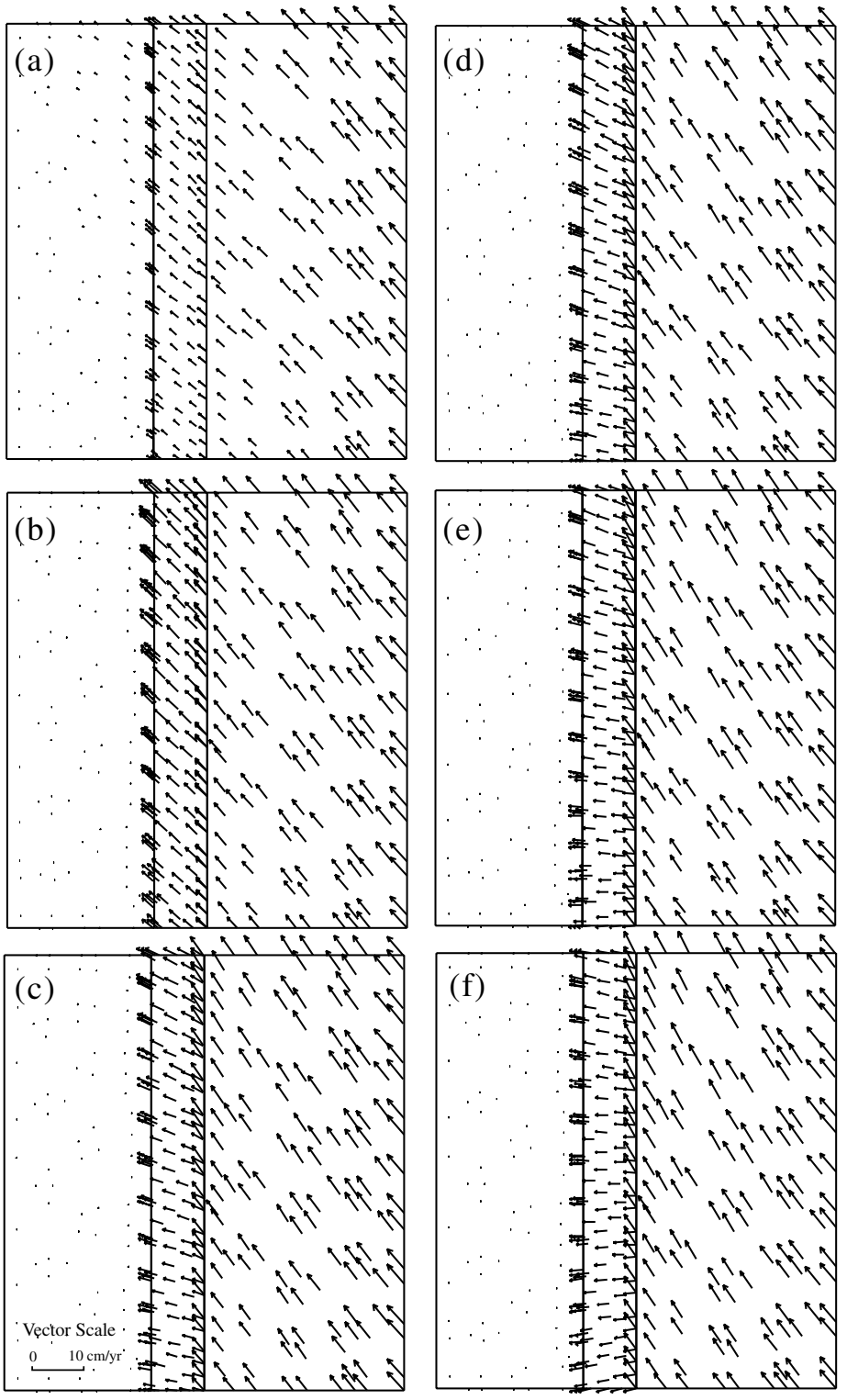
(a)
(b)
(c)
(d)
(e)
(f)
Vector Scale
0 10 cm/yr

data. The uncertainties in friction coefficients discussed below come from these variations. Our models predict that on the eastern fault, between the Coastal Range and the Pinanshan Conglomerate massif, both the dip-slip and strike-slip components increase as the friction coefficient decreases (Fig. 8a). Along the western fault, between the Pinanshan Conglomerate massif and the Central Range, the dip-slip increases as the friction coefficient decreases, but the proportion of strike-slip slip decreases. Remarkably, as the coefficient of friction becomes larger than 0.8, there is no significant strike-slip on the eastern fault. According to our results, the strike-slip and dip-slip are 20.5 and 3.6 mm/yr, respectively, on the eastern fault when an effective friction coefficient is 0.27. This shows that the present-day oblique convergence around the eastern fault accounts for about one tenth of the total fault-normal shortening, but as much as three fifths of the strike-slip shear.

Along the western fault, the strike-slip and dip-slip are 6.1 and 21.2 mm/yr as the effective coefficient of friction is 0.27 (Fig. 8b). As the effective coefficient increases to 1.0, the strike-slip and dip-slips are 16.3 and 15.2 mm/yr, respectively. Both predicted fault-normal shortenings are thus larger than those calculated from geodetic data by Lee et al. (1998). Note that our models ignore by definition the effects of possible internal deformation across the block of the Pinanshan Conglomerate massif.

Not surprisingly, the total displacement rate increases when the coefficient of friction decreases (Fig. 8c). With boundary conditions chosen as function of the GPS data (Fig. 2c), our models predict an average displacement rate of about 33 mm/yr towards N318°E for a range of reasonable values. This result is not surprising, but highlights the prominent role of the LVF as the major kinematic discontinuity in the Taiwan collision belt.

We aimed at taking advantage of the partitioning phenomenon to better constrain the friction parameters on the main faults. The variations of displacement vectors in fault planes are quite significant. The model that provides the best result for the eastern fault has an effective coefficient of friction of 0.27 (Fig. 8). However, along the western fault, the models that provide the best result have a coefficient of friction of about 0.9 (Fig. 8). The dip-slip velocity is however 30% larger than that indicated by the geodetic measurements.

It is important to observe that taking into account not only the relative velocity of the eastern and western blocks but also the relative velocity of the Pinanshan block between them (as revealed by geodetic analyses) brings the additional constraints in the model. This constraint implies a relationship between the coefficients of friction on the western and eastern faults (μ_W and μ_E, respectively). For instance, a model with $\mu_E = 0.27$ and $\mu_W = 0.8$ (Fig. 9a) predicts a strike-slip of 25 mm/yr on the eastern fault and a dip-slip of 19 mm/yr on the western fault. For a model with $\mu_E = 0.1$ and $\mu_W = 0.8$ (Fig. 9b), these values are 20 and 18 mm/yr, respectively. Despite minor variations, the experiments showed that a large coefficient of friction is required on the western thrust relative to the eastern strike-slip fault to account for the geodetic data.

Byerlee (1978) has shown that the laboratory coefficient of friction is remarkably uniform for a wide variety of rock types. Based on in situ stress measurements, Zoback and Healy (1984) proposed a similar result: their coefficients of friction ranged from 0.6 to 1. Friction sliding experiments performed on clay-rich fault gouges of the San Andreas Fault (Morrow et al., 1982) indicated coefficients of friction ranging from 0.15 to 0.55. The friction coefficients required in our models to account for the geodetic data correspond to the latter values for the eastern fault, indicating this major strike-slip fault has a weak mechanical behavior. This is mainly because with a larger friction on this fault, slip would stop and the oblique motion would concentrate on the thrust fault to the west. For the same reason, our models suggest high friction on the western thrust, showing that the observed partitioning has strong implications in terms of relations between the coefficients of friction. How effective friction is influenced by fluid pressure is beyond the

Fig. 7. Plane view (depth 0) of the velocity fields due to a variety of friction coefficients along the major faults, with the same geometry as for Fig. 6a (dips of 45° for western fault and 90° for eastern fault). Friction coefficients are: (a) 1.0; (b) 0.6; (c) 0.4; (d) 0.27; (e) 0.1 and (f) 0.01. Computed shear displacement vectors as a pair of thin arrows. Mechanical properties listed in Table 1.

(a)

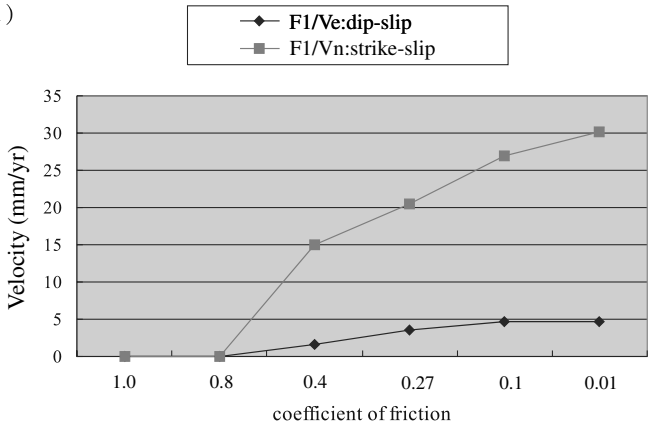

EASTERN FAULT

(b)

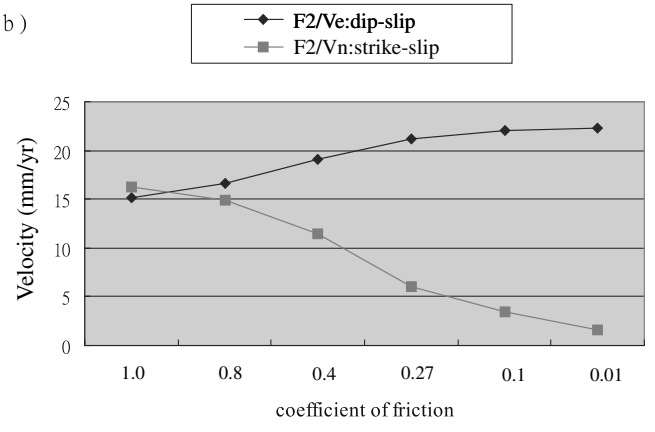

WESTERN FAULT

(c)

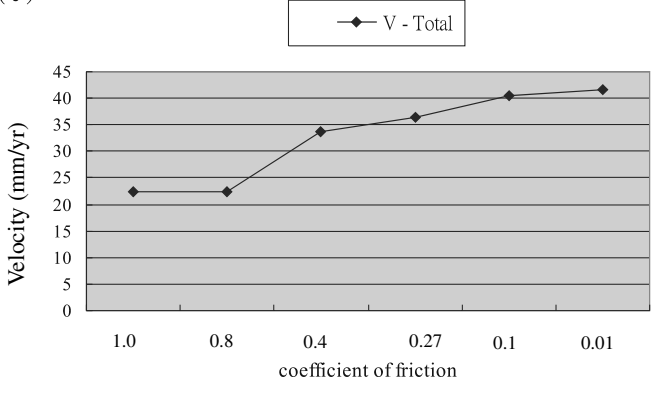

TOTAL

scope of our study; it is worth noting, however, that the Pinanshan Conglomerate is in contact with the mudstone formations of the Lichi Mélange along the eastern strike-slip fault whereas it lies on the metamorphic basement along the western thrust fault.

6. Discussion and conclusions

We aimed at determining how far the direction of convergence applied to model boundaries influences the velocity field inside the model. We thus studied the effect of changes in the direction of plate motion, with azimuths of motion varying from 270 to 360° in seven steps (Fig. 10). These results can be compared with those obtained from the actual azimuth of convergence (Figs. 6, 7 and 9): the velocity field is principally controlled by the geometry (the relative orientation of plate boundary and plate motion). The brittle frictional strength of rocks in the upper crust is significantly affected by the presence of water and other interstitial pore fluids (Byerlee, 1990; Rice, 1992). High fluid pressures appear to be a likely explanation of the shear stresses being lower than those predicted for dry environment. Davis et al. (1983) found that pore fluid pressures in accretionary prism are commonly large fractions of the lithostatic pressure, and therefore strengths are low. Explanations of fault weakness may be based on the assumption of presence at seismogenic depth of frictionally weak fault zone materials, like water-absorbing montmorillonite clays. Another possibility is that they may be based on elevated pore pressure in a fault zone. Pore pressure may be high and approach the normal stress across a major fault zone, resulting in low effective stress and low friction. Such hypotheses received extensive support from geochemical, petrologic and geophysical observations. The stress state within a heavily deformed fault zone weakened by high pore pressure or inherently weak material markedly differs from the stress state in the nearby crust. Molnar (1992) argued that although the attribution of such a partitioning to a weak fault might be correct for some faults, it is not a unique explanation. Richard and Cobbold (1989) designed analog models

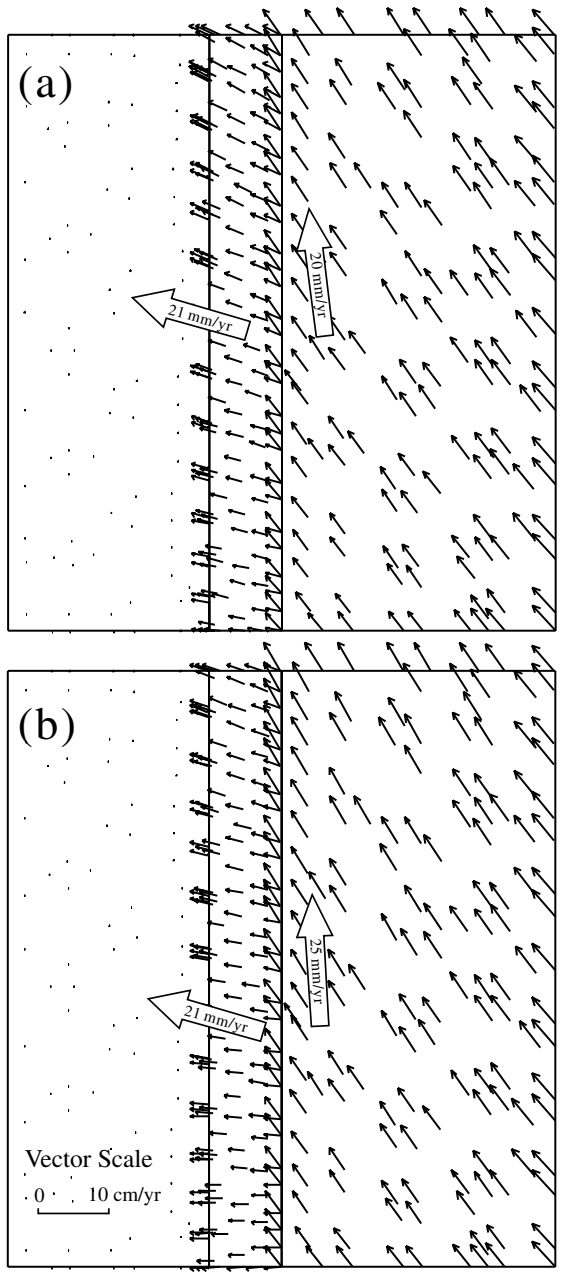

Fig. 9. Plane view (depth 0) of the velocity fields due to a variety of friction coefficients along the major faults. Geometry is the same as for Fig. 6a (dips of 45° for western fault and 90° for eastern fault). Friction coefficients are: (a) $\mu_E = 0.27$ and $\mu_W = 0.8$; (b) $\mu_E = 0.1$ and $\mu_W = 0.8$. Computed shear displacement vectors as a pair of thin arrows.

Fig. 8. The evolution of dip-slip and strike-slip shear across the two major faults in southern Longitudinal Valley. Same block geometry as for Fig. 6a (dips of 45° for western fault and 90° for eastern fault). Velocity as ordinates, coefficient of friction as abscissas. (a) Eastern branch; (b) western branch; (c) total amount of slip.

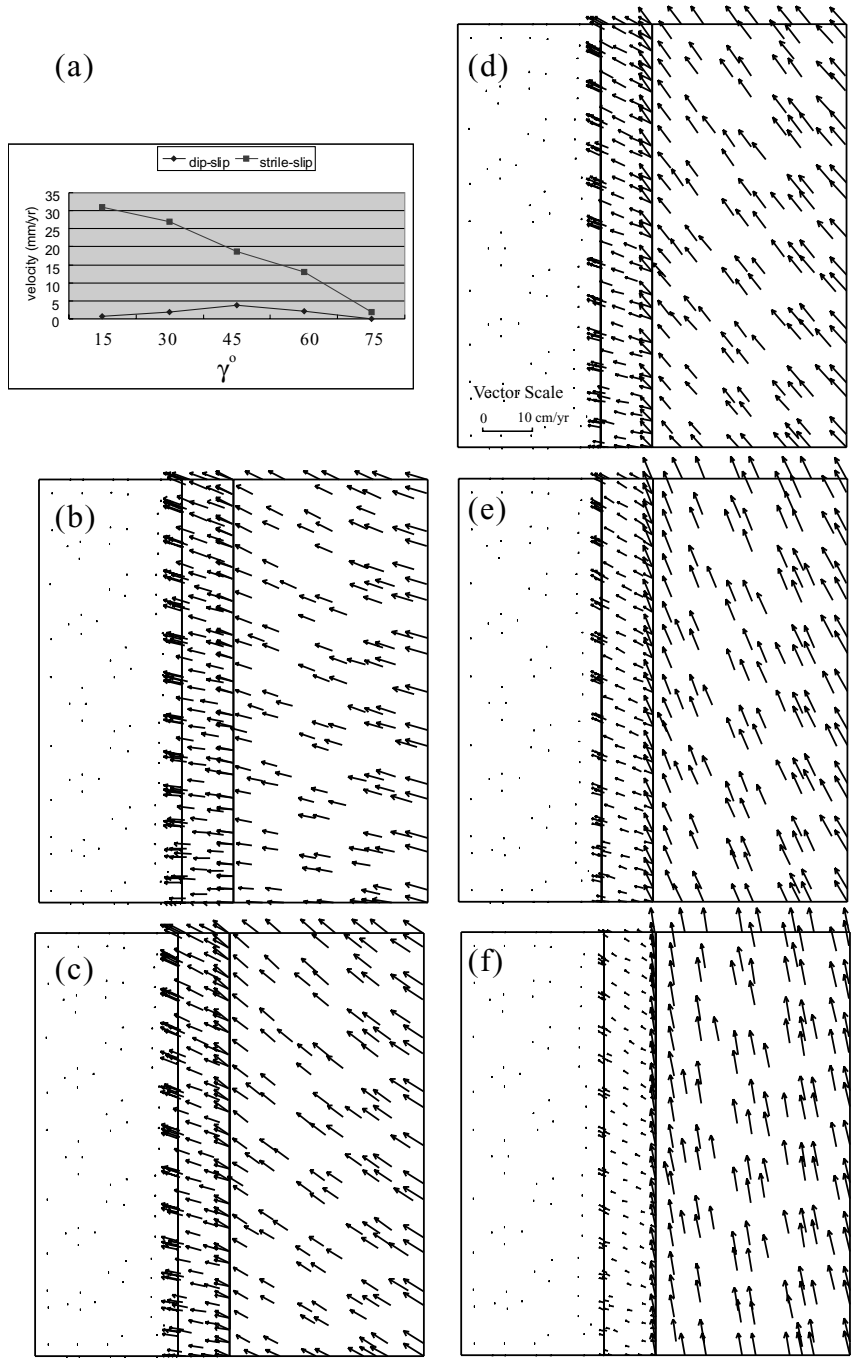

Fig. 10. (a) The dip-slip and strike-slip shear across the eastern fault in the variation of obliquity of block convergence (at an angle γ relative to fault trend) and plane view of the velocity fields due to the influence of the direction of the motion applied to boundary conditions. in southern LVF. Velocity as ordinates, γ as abscissas. Azimuths of convergence: (b) 285°; (c) 300°; (d) 315°; (e) 330°; and (f) 345°. Computed velocity vectors as thin arrows. Same block geometry as for Fig. 6a. Uniform friction coefficient, $\mu = 0.27$. Other mechanical properties listed in Table 1.

Table 1
Numerical values of mechanical and rheological parameters adopted in 3D distinct-element models. For values of μ, see figure captions and discussion in text

	Block material properties	Joint material properties, no sliding	Joint material properties, sliding
Density (kg m^{-3})	2700	–	–
Young's modulus, E (GPa)	60	–	–
Poisson ratio, ν	0.25	–	–
Normal stiffness (GPa/m)	220	220	200
Shear stiffness (GPa/m)	220	220	198
Friction coefficient, μ	–	100	0.01–1.0

implying that the viscous substratum plays a crucial role in partitioning.

In Taiwan, there is a substantial heat flow anomaly that can be attributed to brittle frictional heating. Barr and Dahlen (1989a,b) have used this anomaly to infer the effective coefficient of basal friction. The heat flow data have acceptable fits for effective friction in the range of 0.12–0.46. The basal pore fluid/lithostatic ratio measured in various deep wells near the deformation front is 0.68 (Suppe and Witteke, 1977; Davis et al., 1983). If this value is appropriate along an entire décollement fault, the inferred coefficient of sliding friction is 0.5 (Barr and Dahlen, 1989b). This value is lower than the Byerlee's universal value of 0.85 for most rocks. It is, however, within the range of measured friction values (0.3–0.5) for clay-rich fault gouges (Logan and Rauenzahn, 1987). However, the pore fluid/lithostatic ratio has only been measured in a few deep wells that intersect the décollement fault near the deformation front. Not only there is no direct evidence that the same ratio prevails all along the LVF, but also the differences in behavior between the different fault segments strongly suggest that significant variations occur.

The friction coefficient along faults also depends on lithology, presence of fluids, temperature and other factors (Scholz, 1990). The slip distribution is controlled by the distribution of friction coefficient on the model faults; however, many geological factors also affect the slip distribution, such as heterogeneous properties of surrounding material, non-planar fault segments and discontinuous faults segments (Bürgmann et al., 1994). In our models, we could not analyze the variation of friction on the faults.

Based on 3D modeling with geological structure and geodetic data as major constraints, we could evaluate the role of friction and partitioning in the active transpressive zone of eastern Taiwan. Particular attention was paid to the frictional behavior of geological discontinuities. It was shown that with reasonable values of elastic and frictional parameters the models well account for the actual distribution of displacement velocities. More interestingly, it was shown that to simulate the observed displacement rather tight bounds are required in terms of the coefficients of friction for each of the two faults involved in the partitioning, highlighting the prominent role of friction and mechanical weakness in the transpressive boundary of eastern Taiwan.

Acknowledgements

We are grateful to J. Chéry and one anonymous reviewer for constructive and helpful reviews of the manuscript. This research was supported by National Science Council of Taiwan grant NSC 88-2116-M-001-030 and by the France–Taiwan cooperation in Earth Sciences (French Institute in Taipei and NSC). Pertinent comments by J.-P. Burg resulted in drastic simplification and clarification of the paper.

References

Angelier, J., Chu, H.-T., Lee, J.-C., 1997. Shear concentration in a collision zone: kinematics of the active Chihshang Fault, Longitudinal Valley, eastern Taiwan. Tectonophysics 247, 117–144.

Angelier, J., Chu, H.-T., Lee, J.-C., Hu, J.-C., 2000. Active faulting and earthquake risk: the Chihshang Fault case, Taiwan. J. Geodyn. 29, 151–185.

Barr, T.D., Dahlen, F.A., 1989a. Brittle frictional mountain building 2. Thermal structure and heat budget. J. Geophys. Res. 94, 3923–3947.

Barr, T.D., Dahlen, F.A., 1989b. Constraints on friction and stress in the Taiwan fold-and-thrust belt from heat flow and geochronology. Geology 18, 111–115.

Barrier, E., Angelier, J., Chu, H.-T., Teng, L.S., 1982. Tectonic analysis of compressional structure in an active collision zone: the deformation of the Pinanshan Conglomerates, eastern Taiwan. Proc. Geol. Soc. China 25, 123–138.

Bürgmann, R., Pollard, D.D., Martel, S.J., 1994. Slip distribution on faults: Effects of stress gradients, inelastic deformation, heterogeneous host-rock stiffness, and fault interactions. J. Struct. Geol. 16, 1675–1690.

Byerlee, J., 1978. Friction of rocks. Pure Appl. Geophys. 116, 615–626.

Byerlee, J., 1990. Friction, over pressure and fault normal compression. Geophys. Res. Lett. 17, 2109–2112.

Davis, D., Suppe, J., Dahlen, A.F., 1983. Mechanics of fold and thrust belts and accretionary wedges. J. Geophys. Res. 88, 1153–1172.

Dupin, J.-M., Sassi, W., Angelier, J., 1993. Homogeneous stress hypothesis and actual fault slip: a distinct-element analysis. J. Struct. Geol. 15, 1033–1043.

Fitch, T.J., 1972. Plate convergence, transcurrent faulting and internal deformation adjacent to Southeast Asia and Western Pacific. J. Geophys. Res. 77, 4432–4460.

Harper, T.R., Last, N.C., 1990. Response of fractured rock subject to fluid injection. Part III. Practical application. Tectonophysics 172, 53–65.

Hart, R., Cundall, P.A., Lemos, J., 1988. Formulation of a three dimensional distinct-element model. Part II. Mechanical calculations for motion and interaction of a system composed of many polyhedral blocks. Int. J. Rock Mech. Min. Sci., Geomech. Abs. 25, 117–125.

Hofmann-Wellenhof, B., Lichtenegger, H., Collins, J., 1997. Global Position System: Theory and Practice. Springer, New York, 389 pp..

Hu, J.-C., Angelier, J., Yu, S.-B., 1997. An interpretation of the active deformation of southern Taiwan based on numerical simulation and GPS studies. Tectonophysics 274, 145–169.

Hu, J.-C., Yu, S.-B., Angelier, J., Chu, H.-T., 2001. Active deformation of Taiwan from GPS measurements and numerical simulations. J. Geophys. Res. (in press).

Lee, J.-C., Angelier, J., 1993. Localisation des déformations actives et traitements des données géodésiques: l'example de la faille de la Vallée Longitudinal, Taïwan. Bull. Soc. Géol. Fr. 164, 533–570.

Lee, J.-C., Angelier, J., Chu, H.-T., Yu, S.-B., Hu, J.-C., 1998. Plate-boundary strain partitioning along the sinistral collision suture of the Philippine and Eurasian plates: analysis of geodetic data and geological observation. Tectonics 17, 859–871.

Logan, J.M., Rauenzahn, K.M., 1987. Frictional dependence of gouge mixtures of quartz and montmorillonite on velocity, composition and fabric. Tectonophysics 144, 87–108.

Molnar, P., 1992. Brace-Goetze strength profiles, the partitioning of strike-slip and trust faulting at zone of oblique convergence, and the stress–heat flow paradox of the San Andreas Fault. In: Evans, B., Wong, T.-F. (Eds.), Fault Mechanics and Transport Properties of Rocks. Academic Press, London, pp. 435–459.

Mount, V.S., Suppe, J., 1987. State of stress near the San Andreas Fault: implications for wrench tectonics. Geology 15, 1143–1146.

Morrow, C.A., Shi, L.Q., Byerlee, J.D., 1982. Strain hardening and strength of clay-rich fault gouges. J. Geophys. Res. 87, 6771–6780.

Page, B.M., Suppe, J., 1981. The Pliocene Lichi melange of Taiwan; its plate-tectonic and olistostromal origin. Am. J. Sci. 281, 193–227.

Rice, J.R., 1992. Fault stress states, pore pressure distribution, and the weakness of the San Andreas Fault. In: Evans, B., Wong, T.-F. (Eds.), Fault Mechanics and Transport Properties of Rocks. Academic Press, London, pp. 475–503.

Richard, P., Cobbold, P., 1989. Structures en fleur positives et décrochement crustaux: modélisation analogique et interprétation méchanique. C. R. Acad. Sci. Paris, Série II 308, 553–560.

Scholz, C.H., 1990. The Mechanics of Earthquakes and Faulting. Cambridge University Press, New York.

Suppe, J., Witteke, J.H., 1977. Abnormal pore fluid pressure in relation to stratigraphy and structure in the active fold-and-thrust belt of northwestern Taiwan. Pet. Geol. Taiwan 14, 11–24.

Turcotte, D.L., Schubert, G., 1982. Geodynamics, Application of Continuum Physics to Geological Problems. Wiley, New York, 450 pp..

Yu, S.-B., Jackson, D.D., Yu, G.-K., Liu, C.-C., 1990. Dislocation model for crustal deformation in the Longitudinal Valley area, eastern Taiwan. Tectonophysics 183, 97–109.

Yu, S.-B., Yu, G.-K., Kuo, L.-C., Lee, C., 1992. Crustal deformation in the southern Longitudinal Valley area, eastern Taiwan. J. Geol. Soc. China 35, 219–230.

Yu, S.-B., Chen, H.-Y., Kuo, L.-C., 1997. Velocity field of GPS stations in the Taiwan area. Tectonophysics 274, 41–59.

Zoback, M.D., Healy, J.H., 1984. Friction, faulting, and "in situ" stress. Ann. Geophys. 2, 689–698.